DRAFT VERSION FEBRUARY 24, 2012
Preprint typeset using LaTeX style emulateapj v. 11/26/03

arXiv:1110.2833v3 [astro-ph.CO] 23 Feb 2012

STELLAR POPULATIONS OF HIGHLY MAGNIFIED LENSED GALAXIES: YOUNG STARBURSTS AT $Z \sim 2$.

EVA WUYTS[1,2], JANE R. RIGBY[3], MICHAEL D. GLADDERS[1,2], DAVID G. GILBANK[4], KEREN SHARON[2], MEGAN B. GRALLA[1,2], MATTHEW B. BAYLISS[1,2]

Draft version February 24, 2012

ABSTRACT

We present a comprehensive analysis of the rest-frame UV to near-IR spectral energy distributions and rest-frame optical spectra of four of the brightest gravitationally lensed galaxies in the literature: RCSGA 032727-132609 at $z = 1.70$, MS1512-cB58 at $z = 2.73$, SGAS J152745.1+065219 at $z = 2.76$ and SGAS J122651.3+215220 at $z = 2.92$. This includes new Spitzer imaging for RCSGA0327 as well as new spectra, near-IR imaging and Spitzer imaging for SGAS1527 and SGAS1226. Lensing magnifications of 3-4 magnitudes allow a detailed study of the stellar populations and physical conditions. We compare star formation rates as measured from the SED fit, the Hα and [O II] λ3727 emission lines, and the UV+IR bolometric luminosity where 24 μm photometry is available. The SFR estimate from the SED fit is consistently higher than the other indicators, which suggests that the Calzetti dust extinction law used in the SED fitting is too flat for young star-forming galaxies at $z \sim 2$. Our analysis finds similar stellar population parameters for all four lensed galaxies: stellar masses $3 - 7 \times 10^9\,M_\odot$, young ages ~ 100 Myr, little dust content $E(B-V)$=0.10-0.25, and star formation rates around 20-100 $M_\odot$ yr^{-1}. Compared to typical values for the galaxy population at $z \sim 2$, this suggests we are looking at newly formed, starbursting systems that have only recently started the build-up of stellar mass. These results constitute the first detailed, uniform analysis of a sample of the growing number of strongly lensed galaxies known at $z \sim 2$.

Subject headings: galaxies: high-redshift, strong gravitational lensing, infrared: galaxies

1. INTRODUCTION

Recent years have seen a significant rise in the number of known gravitationally lensed galaxies at $z = 1 - 3$, both reported from well-defined survey searches (Bolton et al. 2006, Cabanac et al. 2007, Hennawi et al. 2008, Lin et al. 2009, Gladders et al. 2011 in preparation) and from serendipitous discoveries (Allam et al. 2007; Belokurov et al. 2007; Smail et al. 2007). The lensing magnification grants access to high signal-to-noise photometric and spectroscopic observations over a wide range of wavelengths and creates unique opportunities for very detailed study of the stellar populations, dynamics and physical conditions of star-forming galaxies at $z \sim 2$, complementing statistical studies of large samples of unlensed star-forming galaxies at these redshifts (e.g. Shapley et al. 2005, Erb et al. 2006a, Daddi et al. 2007, Reddy et al. 2010). Today, these studies are limited by systematic uncertainties related to the recipes used to estimate physical parameters such as metallicity, dust extinction, star formation rate and star formation history. Until the era of extremely large telescopes, lensed galaxies provide unique opportunities to increase our physical understanding of the composition and assembly history of stellar populations during this period of peak star formation in the Universe.

So far most lensing systems have been studied individually, based on different follow-up observations and analysis techniques. To take advantage of the growing number of known strongly lensed sources, it is crucial to invest in a uniform study of their properties. In this paper we present a full analysis of multi-wavelength photometry and rest-frame optical spectroscopy of four of the brightest distant lensed galaxies known to date. RCSGA 032727-132609 was recently discovered in the Second Red-Sequence Cluster Survey (Gilbank et al. 2011); initial analysis of optical/near-IR photometry and construction of a lens model for the foreground galaxy cluster are described in Wuyts et al. (2010). Rest-frame optical spectroscopy from Keck/NIRSPEC is presented in Rigby et al. (2011). This paper adds Spitzer imaging to the SED to probe the rest-frame near-IR. MS1512-cB58 has been studied extensively since its discovery (Yee et al. 1996) and a multitude of photometric and spectroscopic data is available for this system (Ellingson et al. 1996; Teplitz et al. 2000; Siana et al. 2008). SGAS J152745.1+065219 and SGAS J122651.3+215220 are part of the SDSS Giant Arcs Survey (Bayliss et al. 2011); optical photometry and lens models are reported in Koester et al. (2010). Here we present near-IR and Spitzer imaging as well as rest-frame optical spectra for both sources. We will refer to these galaxies as RCSGA0327, cB58, SGAS1527 and SGAS1226.

The paper is organized as follows. §2 describes the near-IR and Spitzer imaging and the rest-frame optical spectroscopy. The methods used for the photometric analysis and spectral energy distribution modeling, as well as the various reddening and star formation rate diagnostics are discussed in §3. §4 presents the physical conditions and stellar populations of the lensed galaxies as derived from these methods. We adopt a flat cosmol-

* Based in part on observations collected at the 3.5 m Apache Point Observatory telescope in New Mexico, which is owned and operated by the Astrophysical Research Consortium

[1] Department of Astronomy and Astrophysics, University of Chicago, 5640 S. Ellis Av., Chicago, IL 60637
[2] Kavli Institute for Cosmological Physics, University of Chicago, 5640 South Ellis Avenue, Chicago, IL 60637
[3] Observational Cosmology Lab, NASA Goddard Space Flight Center, Greenbelt, MD 20771
[4] Department of Physics and Astronomy, University of Waterloo, Waterloo, Ontario, N2L 3G1, Canada

ogy with $\Omega_M = 0.3$ and $H_0 = 70\,\mathrm{km\,s^{-1}\,Mpc^{-1}}$. All magnitudes are quoted in the AB system.

2. OBSERVATIONS AND DATA REDUCTION

2.1. *Imaging*

Optical and near-IR photometry of RCSGA0327 and optical photometry of SGAS1527 and SGAS1226 are taken from their respective discovery papers (Wuyts et al. 2010; Koester et al. 2010). For cB58, we take optical and near-IR photometry from Ellingson et al. (1996) and Spitzer photometry from Siana et al. (2008). Here we present new Spitzer imaging for RCSGA0327 as well as new near-IR and Spitzer imaging for SGAS1527 and SGAS1226.

We observed SGAS1527 and SGAS1226 with the 3.5 m telescope at the Apache Point Observatory (APO) in New Mexico in the J-, H- and K_s-bands during four half nights on 2010 January 30, February 24, March 4 and March 29 with seeing of 0.″7-0.″9. A pipeline of standard IRAF[1] tasks is used to sky-subtract and stack the dithered images, giving total integration times of 3600 s - 4500 s - 3600 s in J - H - K_s for SGAS1527 and 3600 s - 3150 s - 2700 s in J - H - K_s for SGAS1226.

IRAC (Fazio et al. 2004) and MIPS (Rieke et al. 2004) observations of RCSGA0327 and SGAS1527 were obtained through Spitzer program 50823 (PI: M. D. Gladders). RCSGA0327 was observed for 600 s in all four IRAC bands (3.6/4.5/5.8/8.0 μm) and 700 s in MIPS 24 μm; SGAS1527 was observed for 3000 s in all IRAC bands and 1300 s at 24 μm. 600 s warm IRAC observations of SGAS1226 at 3.6 and 4.5 μm were obtained through Spitzer program 70154 (PI: M. D. Gladders). The data is reduced with the MOPEX software distributed by the Spitzer Science Center (SCC) and drizzled to a finer pixel scale of 0.″5 pix^{-1} for IRAC and 1.″5 pix^{-1} for MIPS.

2.2. *Rest-frame optical spectroscopy*

Keck/NIRSPEC rest-frame optical spectra were published for cB58 by Teplitz et al. (2000) and for RCSGA0327 by Rigby et al. (2011). Here we present new spectra for SGAS1527 and SGAS1226.

We observed SGAS1527 and SGAS1226 with the NIRSPEC spectrograph (McLean et al. 1998) on the Keck II telescope on the night of 2010, February 4. The weather was clear, and the seeing was measured as 0.85″ and 0.45″ when the telescope was focused during the night. We used the low-resolution mode and the 0.76″ × 42″ slit which was rotated to position angles of 112° and 121° East of North, respectively, to maximize coverage of each arc. Finder charts showing the location of the slit on each target are given in Figure 1. The targets were acquired by offsetting from the brightest cluster galaxy on the near-IR slit-viewing camera; target acquisition was verified by direct imaging with this camera. The targets were nodded along the slit in an AB pattern, with exposures of 600 s. Table 1 summarizes the filters and total integration times. For SGAS1527, the default grating angles were used, but for SGAS1226 the grating angles were adjusted to give the wavelength ranges reported. The A0V stars 7 Ser and HD 109055 were observed every hour as telluric standards for SGAS1527 and SGAS1226 respectively. In addition, V. Tilvi and J. Rhoads of the Arizona State University have kindly obtained additional spectra of SGAS1527 on 2010, September 17, with the same setup. The A0V star HD 12021, observed 10 hr later, is used as a telluric standard. Due to the time delay, the absolute fluxing in this bandpass should not be trusted.

TABLE 1. SPECTROSCOPIC OBSERVATION LOG.

source	filter	time s	wavelength range μm
SGAS1527	NIRSPEC-4	1800	1.302–1.585
	NIRSPEC-6	3000	1.770–2.190
	NIRSPEC-7	1620	2.242–2.521
SGAS1226	NIRSPEC-5b	1800	1.447–1.730
	NIRSPEC-7b	3000	1.864–2.285

The spectra are reduced with the *nirspec_reduce* package written by G. D. Becker. The data reduction, fluxing, and line-fitting procedures are described in Rigby et al. (2011). Solar abundances are taken from Table 1 of Asplund et al. (2009). The reduced spectra are plotted in Figures 2 and 3; line fluxes are reported in Table 2. At observed wavelengths where the Earth's atmosphere has very little transmission, small mismatches in airmass and precipitable water vapor (PWV) between the telluric and the science target can have a large effect on the flux calibration. To quantify this, Table 2 reports the expected atmospheric transmission[2] for each detected emission line integrated over the gaussian line width as given in §4.1. The quoted uncertainty combines the measurement uncertainty in the line widths, the systematic uncertainty in PWV and the systematic uncertainty from a 0.1 airmass mismatch between the telluric and science target. Subsequent calculations involving line fluxes will take into account both the 1σ flux uncertainties and the fractional uncertainty on the atmospheric transmission.

3. METHODS

3.1. *Photometry*

The photometric analysis of the imaging data follows the method detailed in Wuyts et al. (2010). In short, the data are transformed to a common reference and pixel scale and empirical, normalized point spread functions (PSF) are created for each image. We define object apertures by tracing a curve along the extended source and convolving it with the appropriate PSF. A series of apertures of increasing radial extent are defined as isophotes of this convolution. The apertures can be very much non-circular and are described by equivalent radii based on circular apertures that extend to the same isophotes.

[1] IRAF (Image Reduction and Analysis Facility) is distributed by the National Optical Astronomy Observatories, which are operated by AURA, Inc., under cooperative agreement with the National Science Foundation.

[2] The atmospheric transmission is based on the model absorption spectra for Mauna Kea published by the Gemini Observatory: http://www.gemini.edu/sciops/telescopes-and-sites/observing-condition-constraints/ir-transmission-spectra. The PWV at the time of observations was derived from historical atmospheric opacity data at http://puuoo.caltech.edu/.

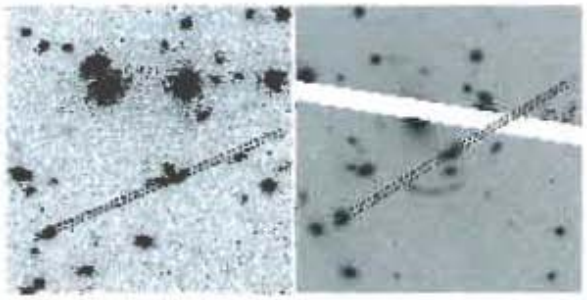

FIG. 1.— Finder charts showing NIRSPEC slit positions for SGAS1527 *(left)* and SGAS1226 *(right)*, both 45 × 45″. The CFHT Megacam r-band image of SGAS1527 and the Gemini GMOS i-band of SGAS1226 (Koester et al. 2010) are overplotted with the NIRSPEC 0.76″ × 42″ longslit at position angles of 112° and 121°East of North respectively. The missing region in the i-band image of SGAS1226 is due to the GMOS chip gap.

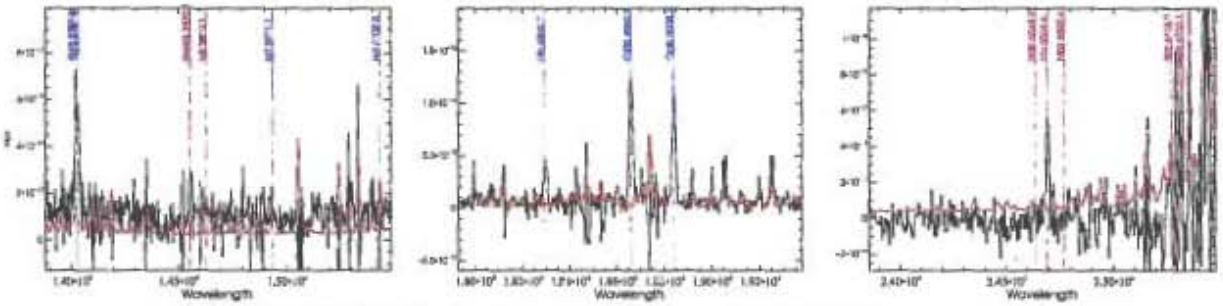

FIG. 2.— NIRSPEC spectra for SGAS1527. The fluxed spectra are plotted in black, with the 1σ error spectrum in red. The X-axis shows observed wavelength in Angstroms; the Y-axis shows observed flux in units of erg s^{-1} cm^{-2}. Blue labels mark detected emission lines as well as lines for which we measure upper limits.

TABLE 2. MEASURED LINE FLUXES.

line ID	λ_{obs} μm	flux 10^{-16} erg s^{-1} cm^{-2}	atm trans
	SGAS1527 - Filter N4		
[OII] 3727	1.40208	11±1	0.54±0.08
[NeIII] 3869	1.45578	4±1	0.62±0.07
	SGAS1527 - Filter N6		
Hβ	1.82932	9±2	0.17±0.08
[OIII] 4959	1.86616	20.0±0.2	0.23±0.08
[OIII] 5007	1.88397	18.0±0.3	0.64±0.08
	SGAS1527 - Filter N7		
Hα	2.46925	10±3	0.82±0.03
	SGAS1226 - Filter N5b		
[OII] 3727	—	9.6±0.7	0.76±0.06
	SGAS1226 - Filter N7b		
Hβ	1.90895	1.8±0.4	0.55±0.09
[OIII] 4959	1.94697	4.5±0.7	0.74±0.04
[OIII] 5007	1.96641	13±4	0.67±0.03

We use the GALFIT package (version 3.0, Peng et al. 2010) to fit Sersic profiles to neighboring galaxies that fall within the object apertures and subtract these from the images. Accurate masking of neighboring galaxies becomes very important for the Spitzer data due to the extended, non-circular PSFs of the IRAC and MIPS instruments. We have found the most robust masking method to be based on cross-convolution. This consists of convolving the Spitzer data with the PSF of a chosen optical band and similarly convolving the optical GALFIT models of neighboring sources with the relevant Spitzer PSF. These convolved models are scaled as needed and subtracted from the convolved Spitzer image.

We measure magnitudes at an equivalent radius of twice the FWHM of the image. The optical and near-IR data are aperture-corrected to an equivalent radius of 6″ based on the curve of growth of the PSF reference star. In Wuyts et al. (2010), we convolved all optical and near-IR images of RCSGA0327 to the spatial resolution of the H-band, which presents the worst seeing over the 9 optical/near-IR bands, in order to measure flux from the same physical region of the source in all bands. This is not repeated here; by aperture correcting final magnitudes to an equivalent radius of 6″, the total source flux in each band is measured, regardless of prior PSF-matching. We have reanalyzed the data for RCSGA0327 without matching the PSFs and find final magnitudes consistent with the photometry reported in Wuyts et al. (2010), within the 1σ uncertainties. The aperture corrections for the IRAC data are applied as detailed in the IRAC handbook[3], the correction for the MIPS data is calculated from a Tiny Tim model of the 24 μm PSF. The MIPS photometry also requires a color correction of -0.04 mag, as stated in the MIPS handbook[4] (assuming $f_\nu \sim \nu^{-2}$). We derive limiting magnitudes for a few non-detections in the Spitzer data: the counter-

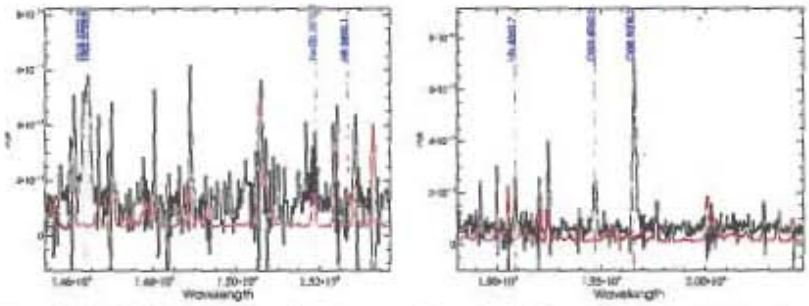

FIG. 3.— NIRSPEC spectra for SGAS1226. The fluxed spectra are plotted in black, with the 1σ error spectrum in red. The X-axis shows observed wavelength in Angstroms; the Y-axis shows observed flux in units of erg s^{-1} cm^{-2}. Blue labels mark detected emission lines as well as lines for which we measure upper limits.

image of RCSGA0327 is not detected at 5.8 and 8.0 μm, and SGAS1527 is not detected at 24 μm. We convolve the image of the source in a chosen optical band with the relevant Spitzer PSF, scale it and manually insert it into the convolved Spitzer image at 100 random positions away from real sources. Limiting magnitudes are determined from the scaling where SExtractor (Bertin & Arnouts 1996) detects 90% of these mock objects at 3σ.

Final magnitudes are corrected for galactic extinction (Schlegel 1998). Photometric uncertainties include Poisson noise, absolute zeropoint uncertainties, uncertainties from the Spitzer aperture corrections as detailed in the instrument handbooks, and uncertainties from the masking of neighboring galaxies; the latter two dominate the total uncertainty. We independently analyze the IRAC and MIPS data for cB58 and find final magnitudes consistent with the photometry in Siana et al. (2008). We choose to use uncertainties twice as large as reported there, to take into account the influence of the halo of the neighboring cD galaxy.

3.2. *Spectral energy distribution modeling*

The available photometry fully characterizes the rest-frame UV to near-IR spectral energy distributions of these galaxies, allowing us to constrain the stellar populations (stellar mass, age, extinction and star formation rate) through a comparison to stellar population synthesis models. The presence of strong emission lines at rest-frame optical wavelengths could affect the broad-band photometry and therefore the SED fit. From the emission line fluxes derived from the rest-frame optical spectroscopy, we estimate the contribution of the strongest emission lines to the H- and K_s-band magnitudes to be at most 5-10%, which does not have a significant effect compared to the estimated photometric errors. Reddy et al. (2010) have also shown that the effect of emission lines on the best-fit age and stellar mass is further reduced when IRAC data (which is unaffected by line contamination at these redshifts) is incorporated.

The fitting procedure, as well as its caveats and degeneracies, is explained in more detail in Wuyts et al. (2010). We use *Hyperz* (Bolzonella et al. 2000) to perform SED fitting at a fixed spectroscopic redshift. The newest Bruzual & Charlot population synthesis models (CB07, kindly made available by the authors - see Bruzual & Charlot (2003)) are used, with a Chabrier initial mass function (Chabrier 2003) and a Calzetti dust extinction law (Calzetti et al. 2000). To reduce the number of degrees of freedom and accompanying degeneracies, we fix the metallicity at $0.4\,Z_\odot$ for all 4 sources, consistent with the abundances indicated by rest-frame optical spectroscopy (see §4.1). SED templates in the literature most often use constant star formation models or exponentially declining models - SFR $\sim e^{-t/\tau}$ - with a wide range of values for the e-folding time τ. The current SFR reported by the SED fitting procedure depends strongly on the assumed star formation history. Other stellar population parameters like dust extinction, age and even stellar mass can be influenced as well; they all work together to produce the observed SED and numerous degeneracies and trade-offs exist. The range of SFHs allowed in the SED fit is therefore not an arbitrary choice. Exponentially declining models assume that we observe the galaxy at its minimum SFR, which is not necessarily justified for star-forming galaxies at z$\sim$2. Maraston et al. (2010) explore inverted τ-models where the star formation rate rises exponentially with time - SFR $\sim e^{+t/\tau}$ - and find a significant improvement in the reproduction of stellar population parameters for a sample of mock star-forming galaxies at $z \sim 2$. For this sample of lensed galaxies, we choose to limit ourselves to a constant star formation history (CSF) as a reasonable average over the galaxy's lifetime and a compromise between exponentially declining and rising SFHs. Erb et al. (2006c) also find the current SFR to be an adequate representation of the past average SFR for their sample of UV-selected galaxies at $z \sim 2$. Additionally, CSF models allow a more robust comparison to other SFR indicators discussed in §3.4, for which the conversions from luminosity are generally based on constant star formation stellar population models.

Now that we have fully defined the input SED models, we have to consider the allowed range of stellar population parameters, specifically the stellar age. The dominant emission of O and B stars in the observed SED of a star-forming galaxy can cause the inferred stellar population parameters to be luminosity-weighted towards very young models, with unrealistically high SFRs and low stellar masses. An often used measure to avoid this

[3] http://ssc.spitzer.caltech.edu/irac/iracinstrumenthandbook/
[4] http://ssc.spitzer.caltech.edu/mips/mipsinstrumenthandbook/

luminosity-weighted bias restricts the age of the stellar population to be larger than the dynamical timescale of the galaxy (Wuyts et al. 2007; Maraston et al. 2010; Reddy et al. 2010). From velocity dispersion and size measurements of $z \sim 2$ LBGs, this is inferred to be ~ 70 Myr (Erb et al. 2006c). We illustrate this bias with histograms of the best-fit ages and star formation rates reported for 1000 mock realizations of the observed SEDs consistent with the photometric uncertainties (Figure 4). There is a clear bimodality of very young models (≤ 70 Myr) and moderately older models (70-200 Myr), which is correlated with a bimodality in the SFR, where the young models require a much higher current SFR to build up a similar stellar mass. Restricting the age to be larger than the dynamical timescale avoids this class of unphysically young stellar populations with extreme SFRs. For cB58, only very young models (ages < 20 Myr) are found for the mock SEDs, due to the lack of a significant Balmer break between the J and H-band photometry from Ellingson et al. (1996). This was also found by Siana et al. (2008), who report a best fit age of $9.3^{+4.7}_{-3.1}$ Myr. However, when the age is restricted to ≥ 70 Myr, more than 90 % of the mock SEDs return a best-fit model with $\chi^2 < 5.0$, which is not unreasonable. We will also show in §4.4 that the extreme SFRs which accompany very young best-fit models for cB58 (300-600 $M_\odot$ yr^{-1} as can be seen from Figure 4) completely disagree with the other SFR indicators.

A further argument in favor of the age restriction comes from the metallicity. When the metallicity is allowed to vary between $0.2\,Z_\odot$, $0.4\,Z_\odot$ and $Z_\odot$, the SED fitting procedure favors a metallicity of $0.2\,Z_\odot$ for all 4 galaxies, lower than indicated by observations of the rest-frame optical spectra. When the age is forced to be ≥ 70 Myr, a metallicity of $0.4\,Z_\odot$ is favored, consistent with the results from rest-frame optical spectroscopy.

Restricting the age of the stellar population limits the sensitivity of the SED fit to the most recently formed stars (on < 70 Myr timescales) and returns more physically meaningful stellar population parameters. A related issue is the presence of an old underlying stellar population (1-2 Gyr timescales), which can contain the majority of a galaxy's stellar mass without emitting enough light to be detected in the observed SED at rest-frame UV and optical wavelengths. The availability of IRAC data at rest-frame near-IR wavelengths greatly increases the leverage, but some contribution of old stars cannot be ruled out from single component SED fitting. Full-scale multi-component SED fitting can address the presence of older stellar populations, but it introduces additional degrees of freedom (the number, relative timing and relative strength of the different star formation episodes), which the data fail to constrain uniquely. We can set an upper limit on the contribution of an old stellar population to the total stellar mass of the galaxies with the extreme case of a very young model, minimally reddened to match the UV spectral slope, combined with a maximally old underlying model (Daddi et al. 2004, Shapley et al. 2005, Wuyts et al. 2010). Specifically, we scale a 10 Myr CSF model to the observed r-band magnitude, subtract this model from the observed SED, and scale the maximally old model ($t = 3$ Gyr for RCSGA0327 and $t = 2$ Gyr for SGAS1527, SGAS1226 and cB58) to match the residual magnitude at 3.6 μm. In this scenario, the stellar mass is largely dominated by the older stellar population, but we find it to be at maximum a factor of 1.7 higher than the single-component mass for all sources (we have corrected the mass of the older stellar population for the mass returned to the ISM by supernovae, this is negligible for ages ~10-100 Myr (Renzini & Ciotti 1993)). This places a conservative constraint on the maximum contribution of old stellar populations to the total stellar mass in these galaxies.

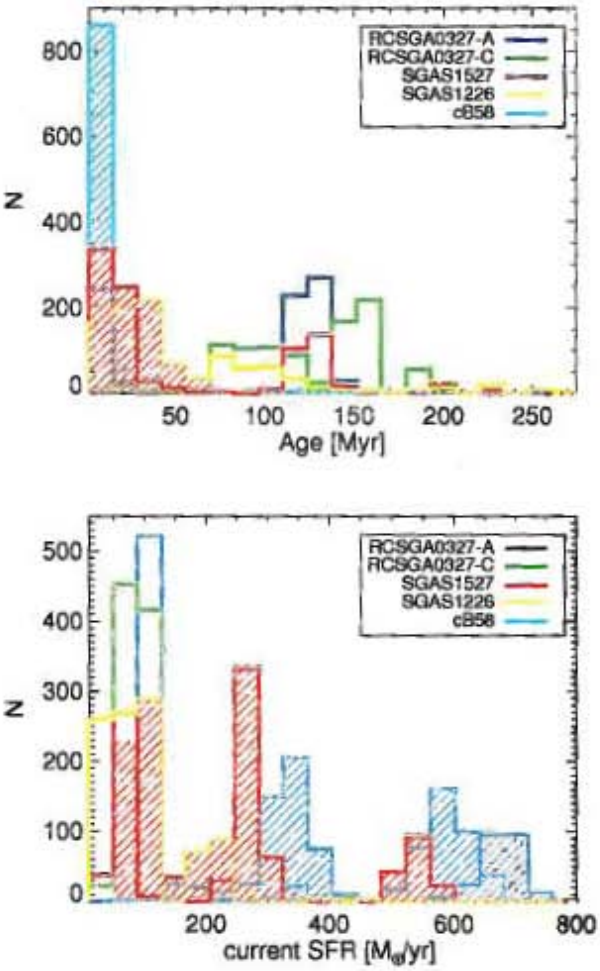

FIG. 4.— Histograms of the best-fit age *(top)* and SFR *(bottom)* for 1000 mock SEDs consistent with the photometric uncertainties. A clear bimodality can be seen. The shaded regions show the best-fit SED models with ages < 70 Myr, which correspond exclusively to the high SFR solutions. This part of parameter space is eliminated when the age is restricted to ≥ 70 Myr.

3.3. *Reddening diagnostics*

The presence of dust in galaxies causes reddening. Since the stars and the ionized gas are not necessarily found in the same locations within a galaxy, the stellar light and the nebular emission lines may not experience the same reddening. In local star-forming galaxies, Calzetti et al. (1994) found the reddening of the nebular lines to be a factor of ~ 2 higher than the reddening

of the stellar continuum. At $z \sim 2$, the same effect has been seen for some star-forming galaxies, both lensed and non-lensed (Förster Schreiber et al. 2009; Finkelstein et al. 2009; Bian et al. 2010), but other galaxies show no reddening difference between the stars and ionized gas (Erb et al. 2006c; Hainline et al. 2009).

The SED fitting procedure reports $E(B-V)_s$, the reddening of the stellar light. We add the subscript to differentiate with the reddening experienced by the galaxy's ionized gas, which we will denote as $E(B-V)_g$. This reddening can be derived from the Balmer decrement, the ratio of the Hα to Hβ flux. We assume an intrinsic Balmer decrement of 2.85, obtained for recombination case B, electron density $n_e \leq 10^4\,\mathrm{cm}^3$ and temperature $T \sim 10^4$ K (Osterbrock 1989). When no measure of the Balmer decrement is available, we use the empirical relation between a galaxy's stellar mass and its gas reddening derived at $z \sim 0.1$ from the Stripe 82 subsample of the Sloan Digital Sky Survey (Eq. 9, Gilbank et. al. 2010). This G10 relation has an uncertainty of ~ 0.2 dex on $E(B-V)_g$ at the relevant stellar masses [5]. This empirical relation has not been verified directly at higher redshift, although agreements with 24 μm emission have been found at $z \sim 1$ (Gilbank et al. 2010), but it is clearly preferable to assuming an intrinsic Balmer decrement.

3.4. *Star formation rate diagnostics*

A galaxy's star formation rate can be estimated from several different indicators, the most common of which are the UV continuum emission, sometimes combined with the infrared emission from dust grains heated by absorbed UV photons, and the nebular emission lines from the ionized gas. Rest-frame UV luminosity is straightforward to measure at $z \sim 2$, but the conversion to a SFR depends on the galaxy's stellar population and the luminosity requires a large correction for dust obscuration. Dust corrections can be avoided by including the galaxy's infrared emission, which traces the stellar light absorbed by dust grains, such that the combined UV and IR luminosity captures the total bolometric output from young stars.

Rest-frame optical emission line indicators require a smaller dust correction than the UV continuum, but need to be extrapolated from the regions of the galaxy sampled by the spectroscopic aperture. These aperture corrections are especially important for lensed galaxies, where the arcs are often too extended to be covered by the slit and a precise magnification model is required to extrapolate the observed line emission to the total intrinsic emission of the galaxy. Additionally, in the presence of strong stellar population gradients, the observed region might not be representative of the galaxy as a whole.

Star formation from UV luminosity

Star formation rates based on the UV continuum are easy to obtain at $z \sim 2$. Two or more broadband magnitudes at rest-frame UV wavelengths suffice to measure the UV luminosity and to estimate the dust correction from the UV spectral slope, as established by Meurer et al. (1999) for local starburst galaxies (based on the Calzetti extinction law). However, this method involves considerable uncertainties. The conversion between UV luminosity and SFR depends strongly on the assumed stellar population model, mostly its age and star formation history, causing an uncertainty of at least 0.3 dex in the calibration (Kennicutt 1998). Additionally, estimates of the dust content based on the UV spectral slope suffer from the degeneracy between a galaxy's dust content, its metallicity and the age of its stellar population, where more dust, more metals or older stars will similarly cause a redder spectral slope. The availability of a spectroscopic measurement of the metallicity, combined with multi-wavelength SED fitting with coverage of the age-sensitive 4000Å break addresses both problems by fully characterizing the galaxy's stellar population, including reliable independent estimates of the dust content, metallicity and age. For these reasons, we will only use the SFR reported by the SED fit in our final comparison of SFR indicators in §4.4. However, since multi-wavelength photometry extending redward of the 4000Å break is not straightforward to obtain and metallicity measurements become increasingly uncertain for galaxies at $z > 1$, we also quantify how reliably we can estimate the dust extinction from the UV spectral slope in §4.2.

Star formation from infrared emission.

An independent estimate of the dust extinction can be obtained from a galaxy's infrared luminosity. Dust grains will re-radiate the absorbed UV emission at infrared wavelengths, such that a galaxy's combined UV and IR luminosity is a good proxy for the total bolometric output from its newly formed stars. One caveat is the contribution to the infrared emission from dust heated by old stars. We can reasonably assume this contribution to be negligible for this sample of galaxies, where the observed SEDs are best fitted by young stellar populations and we found strict limits on the presence of older stars (see §3.2). We use the SFR conversion from Bell et al. (2005)[6], which is derived for a ~100 Myr old stellar population with constant star formation.

$$\frac{SFR}{\mathrm{M_\odot yr^{-1}}} = 2.24 \times 10^{-44}(L_{IR} + 1.9L_{1600})\mathrm{erg\ s^{-1}} \quad (1)$$

L_{IR} is the total infrared luminsosity (5-1000 μm) and $L_{1600} = \nu l_{\nu,1600}$. The factor 1.9 accounts for the spectral slope of the stellar population, such that $1.9L_{1600}$ includes all the UV emission.

L_{IR} is preferably evaluated from sufficient infrared and submillimeter data to capture the bulk of the bolometric energy output of the infrared SED. Unfortunately, data at these longer wavelengths is hard to obtain, especially for sources at higher redshift, due to confusion noise and sensitivity limitations. For this sample, 24 μm data exist for RCSGA0327, cB58 and SGAS1527. cB58 has additionally been detected at 70 μm (Siana et al. 2008), 850 μm (van der Werf et al. 2001) and 1200 μm (Baker et al. 2001). Much work has been done to calibrate L_{IR} from observed 24 μm photometry, which traces the mid-IR region (6-12 μm) for galaxies at $z \sim 2$. This wavelength range is dominated by polycyclic aromatic hydrocarbon (PAH) features, which are stochastically heated

[5] Gilbank et al. (2010) use the Kroupa IMF, we convert to the Chabrier IMF with $\log(\mathrm{M_*})_{\mathrm{Chab}} = \log(\mathrm{M_*})_{\mathrm{Kroupa}} - 0.04$

[6] Bell et al. (2005) use the Kroupa IMF, we convert to the Chabrier IMF with $\mathrm{SFR_{Chab}} = 0.88\ \mathrm{SFR_{Kroupa}}$.

by single UV photons. Recent studies have shown that the physical conditions in star-forming galaxies at $z \sim 2$ are similar to those in local star-forming galaxies of significantly lower infrared luminosity (Papovich et al. 2007; Rigby et al. 2008; Rujopakarn et al. 2011a), such that when local infrared SEDs are used to extrapolate the observed 24 μm emission of $z \sim 2$ galaxies, L_{IR} will be overpredicted by factors of 5-10. This is commonly referred to as the mid-IR excess and has been confirmed by recent Herschel results (Elbaz et al. 2010; Nordon et al. 2010). We avoid this bias by using a new prescription for L_{IR}, based on the local IR SED templates from Rieke et al. (2009), adapted to $z \sim 2$ by accounting for the changing physical conditions of higher redshift star-forming regions (Rujopakarn et al. 2011b). This prescription has a systematic uncertainty of 0.1 dex.

Star formation from nebular emission lines.

The luminosity of the Hα recombination line is directly coupled to the incident number of Lyman continuum photons produced by young stars, and hence is proportional to the SFR. Star formation rates derived from dust corrected Hα emission are generally seen as robust and often used as a comparison and/or calibrator for other indicators (e.g. Gilbank et al. 2010, Reddy et al. 2010). When the Hα line is redshifted out of the optical window, the [O II] λ3727 emission line is commonly used as an indicator of star formation. The luminosity of forbidden lines is not directly coupled to the number of ionizing photons, since the excitation depends on the abundance and ionization state of the gas. Gilbank et al. (2010) derived a mass-dependent correction for these effects by calibrating [O II] SFRs against dust-corrected Hα SFRs locally.

We use the conversions from $L_{H\alpha}$ and $L_{[O\ II]}$ to SFR from Kennicutt (1998)[7]. The reddening of the nebular gas $E(B-V)_g$ as derived in §3.3 is used to correct for extinction. For [O II], we also present values of the corrected [O II] SFR following Gilbank et al. (2010)[8]. The size of this correction is relatively small over the mass range of the galaxies.

4. RESULTS

4.1. *Physical conditions from rest-frame optical spectroscopy*

Analysis of the nebular emission lines from rest-frame optical spectroscopy may allow constraints to be placed on extinction, redshift, velocity width, electron density, ionization parameter and metallicity of galaxies. The results for SGAS1527 and SGAS1226 from the spectra presented in §2.2 are summarized below.

- *Extinction*
  We detect two Balmer lines for SGAS1527, Hα and Hβ, in two different filters. Unfortunately, because the N7 observation lacks a contemporary telluric standard, we do not trust the relative fluxing between Hα and Hβ to measure the reddening. Hγ is not covered, and Hδ is lost to a skyline. For SGAS1226 we detect only one Balmer line, Hβ. Hγ and Hδ were covered by the Nirspec-5b filter, but the lines were not detected. Hα is not accessible from the ground. Thus, we are not able to reliably measure an extinction from the Balmer lines for either galaxy.

- *Redshift*
  We fit the nebular redshift of SGAS1527 using the following emission lines: [Ne III] λ3869, Hβ, [O III] λ4959,5007 and Hα. The derived redshift is $z = 2.76195 \pm 0.0002$. The nebular redshift of SGAS1226 is derived from the emission lines of Hβ and [O III] λ4959,5007 and yields $z = 2.9257 \pm 0.0004$. Both redshifts are slightly higher than those reported in Koester et al. (2010), which were based on absorption features. The presence of galaxy outflows of $\sim$ 200 km/s rest-frame can explain these offsets. The emission line redshifts measured here should serve as the systemic redshifts, since one expects the H II regions to be at rest with respect to the stars.

- *Velocity Width*
  We measure velocity widths of bright lines, and compare them to the instrumental resolution as measured from Argon lamp exposures (see Rigby et al. (2011) for more details). Fits to the [O III] λ4959,5007 and Hα lines of SGAS1527 result in $\sigma = 47 \pm 4$ km s^{-1}. For SGAS1226, $\sigma = 100 \pm 20$ km s^{-1} is derived from the [O III] λ4959,5007 lines. Hβ and the [O II] λ3727 doublet do not inform this analysis, since Hβ is too weak for a useful measurement of its linewidth, and since the [O II] λ3727 doublet is not sufficiently resolved for a non-degenerate fit. These values are consistent with the broad range of $\sigma \sim 40-200$ km s^{-1} found at $z \sim 2-3$ (Erb et al. 2006b).

- *Electron density*
  Rigby et al. (2011) derived an electron density from a two-component fit to the flux ratio of the [O II] λ3727 doublet of RCSGA0327. We have attempted this same procedure for SGAS1527 and SGAS1226, but the lower signal-to-noise of the spectra leads to ambiguous fitting results. In SGAS1527, the line profile appears to have two components, but fitting it as such returns unphysically narrow linewidths - half the instrumental resolution at this wavelength. The source of the problem may be the sky line that falls on the bluer line of the doublet. As a result, we cannot simultaneously determine both the doublet ratio and the velocity dispersion σ in the [O II] λ3727 doublet. Instead, we vary σ within the range permitted by the fit to the [O III] λ4959,5007 lines, fitting a doublet ratio for each value. This results in a flux ratio f(3727/3729) $= 1.03 \pm 0.2$. Using the IRAF task stsdas.analysis.nebular.temden, our measurement corresponds to an electron density $n_e = 400^{+260}_{-230}$ cm^{-3} at $T_e = 10^4$ K. Following a similar procedure for SGAS1226, we find a flux ratio of f(3727/3729) $= 0.59 \pm 0.1$. This corresponds to the low-density limit for $T_e = 10^4$ K.

[7] Kennicutt (1998) uses the Salpeter IMF, we convert to the Chabrier IMF with $\mathrm{SFR_{Salp}} = 1.7\ \mathrm{SFR_{Chab}}$.

[8] Gilbank et al. (2010) use the Kroupa IMF, we convert to the Chabrier IMF with $\mathrm{SFR_{Chab}} = 0.88\ \mathrm{SFR_{Kroupa}}$.

Rigby et al. (2011) found a tight constraint of $n_e = 235^{+28}_{-26}$ cm^{-3} (at $T_e = 10^4$ K) for RCSGA0327. They summarize constraints from the literature for the Clone, the Cosmic Horseshoe and J0900+2234 (see Rigby et al. (2011) for references) as a wide range of $n_e = 600 - 5000$ cm^{-3}, with large uncertainties for individual measurements. These constraints are remarkably higher than the low electron densities found for RCSGA0327, SGAS1527 and SGAS1226, which lie closer to the typical densities of local H II regions, $n_e \sim 100\,\mathrm{cm}^{-3}$ (e.g. Zaritsky et al. 1994).

The inverse relation between electron density and size of the H II regions found locally (Kim & Koo 2001) predicts that local H II regions with $n_e \sim 100\,\mathrm{cm}^{-3}$ should have diameters of ~ 8 pc. If this relation holds at $z \sim 2$, $n_e \sim 300\,\mathrm{cm}^{-3}$ as measured on average for RCSGA0327, SGAS1527 and SGAS1226 corresponds to star-forming regions of ~ 3 pc, while $n_e \sim 1000\,\mathrm{cm}^{-3}$ as an average for the Clone, the Cosmic Horseshoe and J0900+2234 implies H II regions as small as 1 pc. However, the uncertainties on the electron density measurements of these latter sources are large; rest-frame optical spectra of similar quality to what we present in this paper and have published for RCSGA0327 (Rigby et al. 2011) is needed for a larger sample of individual star-forming galaxies at $z \sim 2$.

- *Ionization parameter*
  Figure 1 of Kewley & Dopita (2002) illustrates the use of the flux ratio of [O III] λ5007 to [O II] λ3727 as a diagnostic of the ionization parameter. Assuming an oxygen abundance of 20-40% solar (on the Asplund system), Equation 12 of Kewley & Dopita (2002) [9] yields an ionization parameter of $\log U = -2.9$ to -2.7 for SGAS1527 and $\log U = -2.8$ to -2.9 for SGAS1226. This assumes no extinction; an extinction correction lowers the inferred $\log U$. These results increase the number of lensed galaxies for which this diagnostic is measured from four to six. As noted in Rigby et al. (2011), they all have very similar ionization paremeters of $\log U = -2.9$ to -2.7. This is roughly twice as high as $-3.2 < \log U < -2.9$ measured for lower luminosity local galaxies (Moustakas et al. 2006, 2010).

- *Oxygen abundance*
  Unfortunately, the "gold standard" diagnostic of oxygen abundance, [O III] λ4363, is unavailable in either galaxy, due to limited wavelength coverage in SGAS1527 and skyline contamination in SGAS1226. The ratio of [N II] λ6583 to Hα, known as the N2 index, is a commonly-used, reddening-free abundance indicator. Unfortunately, the redshift of SGAS1226 is too high for these lines to be visible in the near-IR windows. The lines are covered in SGAS1527, though [N II] is not detected, limiting us to an upper limit on the oxygen abundance. We simultaneously fit Hα and the two [N II] lines, setting a common linewidth for all three lines that is allowed to vary within the range measured above. The 3σ upper limit is log ([N II] λ6583/Hα) < -0.65, which corresponds to an oxygen abundance of $12 + \log(O/H) < 8.5$ and a metallicity of $< 70\%$ of solar on the Asplund et al. (2009) scale. The 1σ upper limit on the oxygen abundance is $12 + \log(O/H) < 8.3$, which translates to $< 40\%$ of solar.

  The Ne3O2 index, the ratio of [Ne III] λ3869 to [O II] λ3727 is another accessible, reddening-free abundance indicator. Unfortunatley the [Ne III] line is lost to a skyline in the spectrum of SGAS1226. For SGAS1527, the measured ratio of log ([Ne III] λ3869/[O II] λ3727)$= -0.42^{+0.12}_{-0.17}$ yields an abundance of $12 + \log(O/H) = 7.6 \pm 0.2$ via the calibration of Shi et al. (2007). This corresponds to a metallicity of 5-12% of solar on the Asplund et al. (2009) scale. Unfortunately, as Figure 1 of Shi et al. (2007) makes clear, the scatter in this calibration is large, 0.3 dex overall and worse at low ratios of [Ne III]/[O II]. This diagnostic does therefore not prove useful in this regime.

[9] Kewley & Dopita (2002) use the abundances from Anders & Grevesse (1989); we convert to Asplund et al. (2009).

4.2. *Stellar population parameters*

The stellar populations of the lensed galaxies are constrained by the rest-frame UV to near-IR spectral energy distributions. Figure 5 shows the best-fit SEDs for the arc and counter-image of RCSGA0327, cB58, SGAS1527 and SGAS1226 at rest-frame wavelengths. We have investigated whether the small discrepancy between the photometry and the best-fit SED model that can be seen for RCSGA0327, cB58 and SGAS1226 around the 4000Å break can be significantly reduced by allowing exponentially declining SFHs. We find that this is not the case for cB58 and SGAS1226. For these galaxies the discrepancy is due to a tension between our minimum age constraint of 70 Myr (well motivated in §3.2) and the lack of a significant 4000Å break in the observed photometry. For RCSGA0327, SED models with an e-folding time of $\tau = 10 - 50$ Myr provide improved fits to the photometry, shown by the dashed green lines in Figure 5. The current SFR derived from the SED fit depends greatly on the assumed star formation history. For both the arc and the counter-image of RCSGA0327, exponentially declining SFHs with $\tau = 10 - 50$ Myr produce SFRs $< 20\,\mathrm{M}_\odot\,\mathrm{yr}^{-1}$, much smaller than indicated by the other SFR measurements (see §4.4). Recently, Wuyts et al. (2011) have similarly reported the need for a minimum e-folding time of $\log(\tau) = 9.5$ (for CB07models) to avoid SFRs that are underestimated compared to measurements derived from the bolometric luminosity for galaxies out to $z \sim 3$. For the relatively young ages of the lensed galaxies in this sample, such long e-folding times are equivalent to the assumption of constant star formation.

Table 3 reports the stellar population parameters derived from the SED fit. The confidence intervals are estimated from 1000 mock realizations of the observed SEDs which are consistent with the photometric uncertainties, and by varying the age restriction between 50 and 100 Myr. The age t and reddening factor $E(B-V)$ depend solely on the galaxy's colors; the stellar mass and star formation rate have an additional dependence

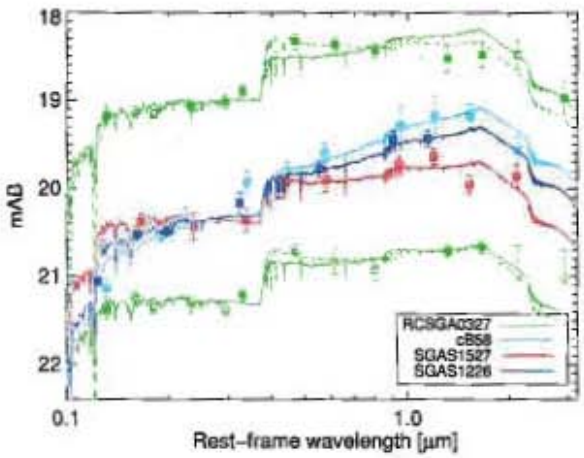

FIG. 5.— Best fit stellar energy distributions for the arc *(top)* and counter-image *(bottom)* of RCSGA0327, cB58, SGAS1527 and SGAS1226 derived from age-restricted CSF models. The dashed green lines show the improved SED fits for both the arc and counter-image of RCSGA0327 when using an exponentially declining SFH with e-folding time τ=10-50 Myr. Photometry datapoints are overplotted with 1σ errorbars.

on the lensing magnification. Based on WFC3/HST images, Sharon et al. (2011) (in preparation) report a magnification factor of 3.0±0.2 for the counter-image of RCSGA0327 and an average magnification of 25.1±3.2 across the giant arc. Koester et al. (2010) report magnification limits of < 15 for SGAS1527 and > 40 for SGAS1226. cB58 is magnified by a factor of 30, with an estimated uncertainty of 30% (Seitz et al. 1998). The magnification uncertainties are included in the reported uncertainties for the stellar mass and SFR.

The stellar populations of all four lensed galaxies are remarkably similar and can be characterized on average with an age ~ 110 Myr, reddening $E(B-V)_s \sim 0.17$, SFR $\sim 65\,M_\odot\ yr^{-1}$ and stellar mass $\sim 5.5 \times 10^9\,M_\odot$. Compared to representative samples of UV-selected star-forming galaxies at $z \sim 2-3$ (Shapley et al. 2001; Erb et al. 2006b; Mannucci et al. 2009; Reddy et al. 2010), these lensed galaxies represent young, starbursting systems with low stellar masses, suggesting they have only recently begun building their stellar population. The same conclusion is reached from a comparison of the UV luminosity and stellar mass to the characteristic luminosity and stellar mass of comparable galaxies at $z \sim 2-3$. Using the characteristic luminosity from Oesch et al. (2010) at $z = 1.5-2.0$ for a comparison to RCSGA0327 and the results from Reddy & Steidel (2009) at $z = 2.7-3.4$ for a comparison to cB58, SGAS1527 and SGAS1226, we find an average brightness of $\sim 2.6\ L_*$. The stellar mass of the sample lies at $\sim 0.08\ M^*_{star}$ when comparing to the characteristic stellar mass found by Marchesini et al. (2009) at $z \sim 2-3$.

We now revisit the issue raised in §3.4 of how reliably one can estimate the dust extinction $E(B-V)_s$ from the UV spectral slope alone. This is relevant for galaxies at $z > 1$, where the photometric and spectroscopic data required to fully characterize the galaxy's stellar population through SED fitting becomes hard to obtain. We use the UV color of the galaxies, derived from the filters that best match the rest-frame 1600Å-2300Å window, to measure the UV spectral slope β ($f_\lambda \sim \lambda^\beta$). The reddening $E(B-V)_s$ derived from β and the relation established by Meurer et al. (1999) for local starburst galaxies is consistently a factor of 1.25-2.0 lower than the value reported by the SED fit. This underestimates the dust-corrected SFR of the galaxies by factors of 2-3.5.

We investigate the origin of this discrepancy by establishing the relation between β and $E(B-V)_s$ for representative CB07 models. For a range of values $E(B-V)_s = [0, 0.3]$ we redden each SED model with the Calzetti dust extinction law and measure the UV spectral slope based on the same filters available to us for each of the four galaxies in the sample (specifically B and r for RCSGA0327, V and I for cB58, r and z for SGAS1527 and r and i for SGAS1226). Since β depends somehat on the exact wavelength window used, this results in four slightly different relations between β and $E(B-V)_s$ for each SED model. Figure 6 shows the Meurer relation in red, offset from the $E(B-V)_s$ values reported from the SED fit (black datapoints). The relations between β and $E(B-V)_s$ for a solar metallicity, 500 Myr old CSF model and a 100 Myr old CSF model with a metallicity of $Z_\odot$ and 0.4 $Z_\odot$ are shown in cyan, blue and green respectively. The 100 Myr, 0.4 $Z_\odot$, CSF model is representative of the average stellar population of the galaxies, and can be seen to agree with the best-fit values for $E(B-V)_s$ from the SED fit. The lower metallicity accounts for much of the discrepancy with the Meurer relation: a 0.4 $Z_\odot$ SED model is intrinsically less red than a solar metallicity SED model and thus requires a larger dust correction to match the same UV spectral slope. In general, this highlights the danger of blindly adopting the Meurer relation to dust-correct the UV continuum emission of high redshift galaxies, without additional information on the age and metallicity of the stellar populations.

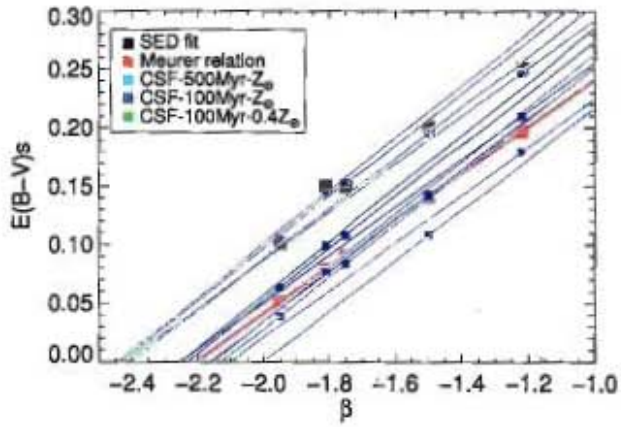

FIG. 6.— The relation between the UV spectral slope β and the reddening $E(B-V)_s$. The local relation established by Meurer et al. (1999) is shown in red. The black datapoints show the galaxies' best-fit $E(B-V)_s$ from the SED fit. The relations we derived for the SED models are shown in cyan, blue and green. The 100 Myr, 0.4 $Z_\odot$, CSF model is representative of the average stellar population of the galaxies and agrees with the results from the SED fit.

TABLE 3. STELLAR POPULATION PARAMETERS.

source	Age (Myr)	$E(B-V)_s$	$\log(M_*/M_\odot)$	SFR ($M_\odot\,yr^{-1}$)
RCSGA0327-A	128±13	0.15±0.035	9.83±0.06	71±12
RCSGA0327-C	143±42	0.10±0.04	9.76±0.05	52±15
cB58	72±18	0.25±0.055	9.69±0.14	82±27
SGAS1527	126±31	0.15±0.05	$> 9.82 \pm 0.04$	$> 71 \pm 16$
SGAS1226	86±41	0.20±0.05	$< 9.54 \pm 0.07$	$< 48 \pm 15$

TABLE 4. EXTINCTION ESTIMATES.

source	$E(B-V)_s$	$E(B-V)_g^{Balmer}$	$E(B-V)_g^{M_*}$
RCSGA0327-A	0.15±0.035	0.20±0.19	0.31±0.18
RCSGA0327-C	0.10±0.04	...	0.29±0.17
cB58	0.25±0.055	0.11±0.10	0.20±0.12
SGAS1527	0.15±0.05	...	0.24±0.14
SGAS1226	0.20±0.05	...	0.15±0.09

Column 1: Reddening of the stellar light from the SED fit
Column 2: Reddening of the nebular gas from the Balmer decrement
Column 3: Reddening of the nebular gas based on the stellar mass as derived by Gilbank et al. (2010)

4.3. *Reddening*

We report the reddening of the stellar light, $E(B-V)_s$ and the reddening of the ionized gas, $E(B-V)_g$ in Table 4. These measures of reddening are important to reliably correct the SFR indicators for dust extinction. $E(B-V)_s$ is taken from the SED fit, $E(B-V)_g$ is estimated from the stellar mass following the local G10 relation (Gilbank et al. 2010, see §3.3). For the giant arc of RCSGA0327 and for cB58, a measurement of the gas reddening can also be made from the Balmer decrement (Rigby et al. 2011; Teplitz et al. 2000) and the independent estimates of $E(B-V)_g$ appear consistent within the 1σ uncertainties. This suggests that the local G10 relation remains valid at $z \sim 2$ and there is mild or no evolution in the dust content of galaxies as a function of mass between these epochs. However, we note that this is only based on two measurements and more work is needed to verify the validity of this local prescription at higher redshift. For RCSGA0327 and cB58, we use the weighted average of both measures of $E(B-V)_g$ to correct the nebular emission line SFR indicators for extinction.

Within the 1σ uncertainties, these reddening measurements cannot conclude whether or not the nebular emission lines experience larger reddening than the stellar light in this sample of star-forming galaxies.

4.4. *Star Formation Rates*

We have outlined 4 different SFR indicators in §3.4 based on the SED fit, the total bolometric luminosity and the Hα and [O II] λ3727 emission lines. The SFR result from the SED fit is reported in §4.2, after being corrected for the lensing magnification (25.1 ± 3.2 for RCSGA0327-A, 3.0 ± 0.2 for RCSGA0327-C, 30 ± 9 for cB58, < 15 for SGAS1527 and > 40 for SGAS1226). We summarize the de-lensed UV and IR luminosities of the galaxies (corrected using the same magnification factors) in Table 5 and use Equation 1 to derive the SFR from the bolometric luminosity.

The emission line luminosities of SGAS1527 and SGAS1226 are derived from the observed fluxes reported in Table 2. As can be seen in Figure 1, the NIRSPEC slit covers the whole source for both galaxies, so we can use the total magnifications of < 15 for SGAS1527 and > 40 for SGAS1226 to calculate the de-lensed luminosities, without additional aperture corrections. Since no measurement of Hα exists for either source (we don't trust the fluxing of SGAS1527 due to a time delay with the observation of the telluric star and for SGAS1226 Hα falls outside the observable window due to its high redshift), we use Hβ and the extinction $E(B-V)_g$ derived from the stellar mass following the G10 relation (see § 4.3) to estimate $L_{H\alpha}$. For cB58, the Hα and [O II] λ3727 luminosities published by Teplitz et al. (2000) are used and corrected for a total magnification of 30 ± 9. For RCSGA0327, we use the emission line measurements from Rigby et al. (2011). Sharon et al. (2011, in preparation) calculate an average magnification of 42.2 ± 5.5 for the area of the arc covered by the NIRSPEC slit. Rigby et al. (2011) recommend using the observed Hβ flux and the Balmer decrement to estimate $L_{H\alpha}$. For all galaxies, de-lensed Hα and [O II] λ3727 luminosities are summarized in Table 5 and the resulting SFRs are dust-corrected using the Calzetti extinction law and $E(B-V)_g$ from § 4.3.

The different SFR indicators are compiled in Table 6 and Figure 7 for easy comparison. For SGAS1527 and SGAS1226, all SFR measurements are upper/lower limits due to the poorly constrained magnification; however on a relative scale, these limits can still be used for a comparison of the different indicators.

The complex lensing signature of RCSGA0327 does not allow a direct comparison of the SFRs between the giant arc and the counter-image. The lens model tells us that the counter-image is a more or less uniformly magnified image of the source plane galaxy. The giant arc on the other hand consists of three merged images of the source galaxy and depending on the location with respect to the lensing caustic, different regions within the source plane galaxy receive very different magnifications (see Sharon et al. 2011, in preparation, for more details). The de-lensed luminosities and derived SFRs of the giant arc are therefore not representative of the source galaxy, and should not be compared directly to the results from the counter-image. Additionally, Sharon et al. 2011 (in preparation) find that the area of the arc observed spectroscopically translates into a very small region of the galaxy in the source plane, which consists of a few highly

TABLE 5. DE-LENSED LUMINOSITIES.

source	L_{1600} 10^{44} erg s^{-1}	L_{IR} 10^{44} erg s^{-1}	$L_{H\alpha}$ 10^{42} erg s^{-1}	$L_{[O\ II]}$ 10^{42} erg s^{-1}
RCSGA0327-A	4.3±0.6	8.4±3.9	5.4±1.4[a]	3.3±0.4[a]
RCSGA0327-C	5.1±0.5	2.4±1.3	...	...
cB58	2.1±0.7	4.9±2.2	2.6±0.8[b]	2.6±0.8[b]
SGAS1527	$> 5.3 \pm 0.4$	$\sim 3.7 \pm 1.7$[c]	$> 14 \pm 8$[d]	$> 4.6 \pm 0.9$
SGAS1226	$< 2.0 \pm 0.1$	...	$< 1.1 \pm 0.4$[d]	$< 1.7 \pm 0.3$

[a]Rigby et al. (2011) - corrected for an average magnification of 42.2 ± 5.5 as calculated by Sharon et al. (2011, in preparation). These luminosities are derived from the area of the giant arc targeted for spectroscopy, which translates into a small region of the galaxy in the source plane (Sharon et al. 2011, in preparation), and are not valid for the whole galaxy.
[b]Teplitz et al. (2000)
[c]SGAS1527 was not detected at 24 μm, the reported luminosity represents a 3σ upper limit, corrected for a lower limit on the magnification of < 15
[d]Hα is derived from Hβ and the Balmer decrement as derived from the stellar mass through the G10 relation (Gilbank et al. 2010)

TABLE 6. STAR FORMATION RATES.

source	SFR_{SED}	SFR_{UV+IR}	$SFR_{H\alpha}$	$SFR_{[O\ II]}$	$SFR_{SED-SMC}$
RCSGA0327-A	71±12	37±9	44±17[a]	48±21[a]	37±6
RCSGA0327-C	52±15	27±4	...	...	39±7
cB58	82±27	20±6	16±6	29±13	38±14
SGAS1527	$> 71 \pm 16$	$\sim 31 \pm 4$[b]	$> 112 \pm 73$	$> 66 \pm 29$	39±4
SGAS1226	$< 48 \pm 15$	...	$< 7 \pm 3$	$< 20 \pm 8$	16±2

[a]These SFRs are derived from the area of the giant arc targeted for spectroscopy, which translates into a small region of the galaxy in the source plane (Sharon et al. 2011, in preparation), and are not valid for the whole galaxy.
[b]SGAS1527 was not detected at 24 μm, the reported luminosity represents a 3σ upper limit, corrected for a lower limit on the magnification of < 15

magnified individual star-forming complexes. The SFRs measured for this area from the Hα and [O II] λ3727 emission lines are not valid for the whole galaxy and we do not include them in our overall comparison of SFR indicators. A future paper will constrain the Hα luminosity of the source galaxy from rest-frame optical spectroscopy of the counter-image.

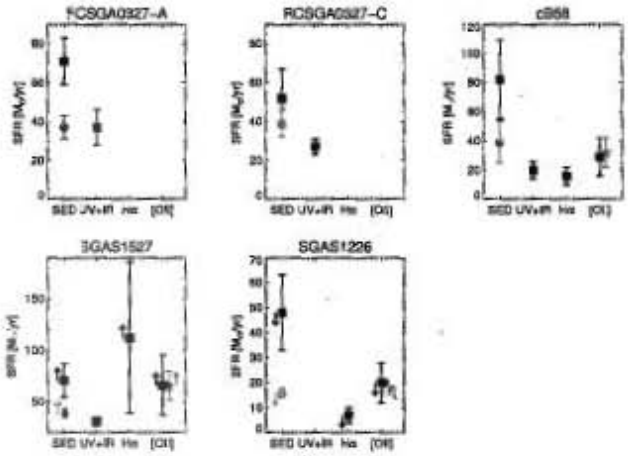

FIG. 7.— Comparison of SFR indicators. The gray stars correspond to the mass-dependent G10 correction for $SFR_{[O\ II]}$ from Gilbank et al. (2010). The SFR derived from the SED fit is overall larger than the other indicators, which suggests that the Calzetti extinction law overpredicts the dust correction for the UV luminosity. The results from an SED fit with the steeper SMC extinction law are shown as gray circles.

Figure 7 shows a general trend where the SFR derived from the SED fit is overall larger than the other indicators (except for SGAS1527). This suggests that the SED fit, and thus the dust-corrected UV continuum emission, overpredicts the star formation rate. A similar result was found for young LBGs (age < 100 Myr) at $z \sim 2$ (Reddy et al. 2010), and for cB58 and the Cosmic Eye (Siana et al. 2009). These authors have suggested that the Calzetti extinction law is not a good representation of the dust geometry in young LBGs at $z \sim 2$ and will significantly overpredict the dust extinction.

The influence of the shape of the extinction law on the dust extinction is commonly illustrated with the Meurer-plot (Meurer et al. 1999), plotting the UV spectral slope β ($f_\lambda \sim \lambda^\beta$) versus the ratio of IR to UV luminosity, which serves as a parametrization of the dust extinction[11]. On this plot, a steeper extinction law results in comparatively more absorption of photons at blue wavelenghts and thus a redder UV spectral slope β for the same extinction. For local starbursts, plotted as little black crosses in Figure 8, the Calzetti extinction law is the best fit (Meurer et al. 1999). Reddy et al. (2010) have shown that at $z \sim 2$, the Calzetti law remains valid for star-forming galaxies with ages > 100 Myr. However, the younger LBGs in their sample, as well as cB58 and the Cosmic Eye, all tend to lie below the Calzetti curve, showing less extinction than would be derived from the UV spectral slope. For these sources, the steeper extinc-

[11] Meurer et al. (1999) define this relation for L_{FIR}, integrated from 40 to 120 μm, where $L_{IR} = 1.75 \times L_{FIR}$ based on the calibration by Calzetti et al. (2000).

tion law derived for the Small Magellanic Cloud (SMC, Prevot et al. 1984) seems to be a better fit. We can add datapoints for the arc and counter-image of RCSGA0327, for SGAS1527 and for our re-analysis of cB58 to this plot. Due to the relatively blue spectral slopes of RCSGA0327 and SGAS1527, these galaxies have limited leverage to distinguish between the different extinction laws.

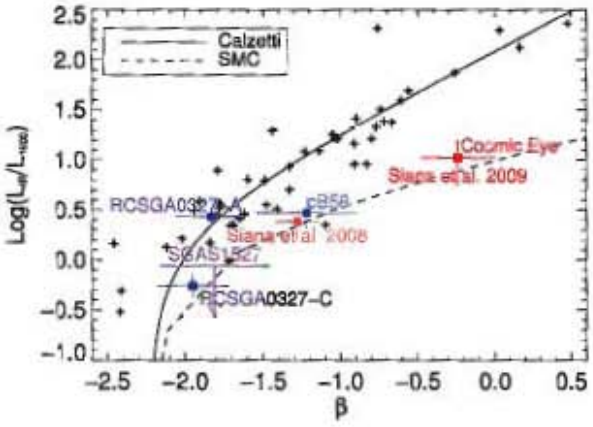

FIG. 8.— Dust attenuation, parameterized as the ratio between IR and UV luminosity, versus rest-frame UV spectral slope β. The measurements of local starburst galaxies are plotted as little black crosses. The best-fit relation corresponds to the Calzetti dust extinction law (Meurer et al. 1999). The steeper SMC extinction law is also shown. The red datapoints for cB58 and the Cosmic Eye are taken from Siana et al. (2008) and Siana et al. (2009) respectively. The relatively blue spectral slopes of RCSGA0327 and SGAS1527 have limited leverage to distinguish between the different extinction laws.

We have repeated the SED fitting with the steeper SMC extinction law. With the exception of cB58, the best-fit SED can not be distinguished from the result obtained with the Calzetti law in terms of the reduced χ^2 of the fit. The improved fit for cB58 was also reported by Siana et al. (2008). The derived SFRs are lower by a factor of 1.3-2 compared to the Calzetti extinction law and therefore in closer general agreement to the other SFR indicators (gray circles in Figure 7). With the SMC law, the stellar mass is consistent with previous results, but the best-fit ages are higher by a factor of ~ 2 and there is no sub-population of very young extreme starbursts, which makes the age restriction to older than 70 Myr unnecessary.

5. SUMMARY

This paper presents a uniform analysis of rest-frame UV to near-IR spectral energy distributions and rest-frame optical spectra for a sample of four of the brightest lensed galaxies at $z \sim 2$. Given the limitations of current facilities, such extensive data collection and detailed analysis of stellar populations and physical conditions would not be possible for individual galaxies at this redshift without the magnification induced by gravitational lensing. SED fits to the rest-frame UV to near-IR photometry result in very uniform stellar population parameters across the sample, which we can characterize as young, bright, starbursting systems with little dust content and low stellar masses. We derive a strict limit on the presence of an older stellar population. Restricting the age of the stellar population to be larger than the dynamical timescale of 70 Myr during the SED fitting is necessary to avoid extreme young starburst models and to obtain metallicities consistent with those found from the rest-frame optical spectroscopy. When the local Meurer relation (Meurer et al. 1999) is used to estimate the dust correction from the UV spectral slope, $E(B-V)_s$ is underestimated by factors of 1.25-2, leading to underestimates of the dust-corrected UV continuum SFR by factors of 2-3.5. This is largely due to the lower metallicity (0.4 $Z_\odot$) of the galaxies. This result cautions the use of the Meurer relation without further characterization of a galaxy's stellar population and motivates efforts to measure metallicities for larger samples of both lensed and field galaxies at $z \sim 2$.

We present SFR estimates based on the SED fit, the UV+IR bolometric luminosity and the Hα and [O II] λ3727 emission lines. The SED fit with the default Calzetti extinction law reports a SFR estimate that is consistently higher than the other indicators. Similar results were found for cB58 and the Cosmic Eye (Siana et al. 2009). This suggests that the Calzetti extinction law is too flat for young star-forming galaxies at $z \sim 2$ and therefore overpredicts the dust extinction. In the diagnostic Meurer plot, the galaxies' spectral slopes are unfortunately too blue to differentiate between the Calzetti law and the steeper SMC extinction law. SED fitting with the SMC law returns SFRs lower by a factor of 1.3-2, bringing this method into general agreement with the other SFR indicators, within the 1σ uncertainties. These results are a first attempt to compare the common SFR indicators in detail for individual galaxies at $z \sim 2$; the comparison would clearly benefit from a larger sample of galaxies.

We thank the referee for useful comments and suggestions that helped improve the quality and presentation of the paper. We are grateful to Vithal Tilvi and James Rhoads for additional observations of SGAS1527 with NIRSPEC. We thank Wiphu Rujopakarn and George Rieke for sharing their new conversions between 24 μm emission and IR luminosity for high redshift galaxies in advance of publication. We thank Brian Siana for helpful discussions. EW acknowledges support from the Carnegie-Brinson Predoctoral Fellowship. Data presented in this paper were partly obtained at the W.M. Keck Observatory from telescope time allocated to the National Aeronautics and Space Administration through the scientific partnership with the California Institute of Technology and the University of California. The Observatory was made possible by the generous financial support of the W.M. Keck Foundation. We acknowledge the very significant cultural role and reverence that the summit of Mauna Kea has always had within the indigenous Hawaiian community. We are most fortunate to have the opportunity to conduct observations from this mountain.

REFERENCES

Adelberger, K. L., Steidel, C. C., Shapley, A. E., Hunt, M. P., Erb, D. K., Reddy, N. A.,& Pettini, M. 2004, ApJ, 607, 226

Allam, S. S., Tucker, D. L., Lin, H., Diehl, H. T., Annis, J., Buckley-Geer, E. J., & Frieman, J. A. 2007, ApJ, 662, L51

Anders, E., & Grevesse, N. 1989, Geochim. Cosmochim. Acta, 53, 197
Asplund, M., Grevesse, N., Sauval, A. J., & Scott, P. 2009, ARA&A, 47, 481
Baker, A. J., Lutz, D., Genzel, R., Tacconi, L. J., & Lehnert, M. D. 2001, A&A, 372, L37
Bayliss, M. B., Hennawi, J. F., Gladders, M. D., Koester, B. P., Sharon, K., Dahle, H., & Oguri, M. 2011, ApJS, 193, 8
Bell, E. F. et al. 2005, ApJ, 625, 23
Belokurov, V. et al. 2007, ApJ, 671, L9
Bertin, E. & Arnouts, S. 1996, A&AS, 117, 393
Bian, F. et al. 2010, ApJ, 725, 1877
Bolton, A. S., Burles, S., Koopmans, L. V. E., Treu, T., & Moustakas, L. A. 2006, ApJ, 638, 703
Bolzonella, M., Miralles, J.-M., Pelló, R. 2000, A&A, 363, 476
Brinchmann, J., Charlot, S., White, S. D. M., Tremonti, C., Kauffmann, G., Heckman, T.,& Brinkmann, J. 2004, MNRAS, 351, 1151
Bruzual, G., Charlot, S. 2003, MNRAS, 344, 1000
Buat, V. 2007, ApJS, 173, 404
Cabanac, R. A., Valls-Gabaud, D., Jaunsen, A. O., Lidman, C., & Jerjen, H. 2005, A&A, 436, L21
Cabanac, R. A., et al. 2007, A&A, 461, 813
Calzetti, D., Kinney, A. L., & Storchi-Bergmann, T. 1994, ApJ, 429, 582
Calzetti, D., Armus, L., Bohlin, R. ., Kinney, A. L., Koornneef, J., & Storchi-Bergmann, T. 2000, ApJ, 533, 682
Calzetti, D. et al. 2005, ApJ, 633, 871
Chabrier, G. 2003, PASP, 115, 763
Chary, R., & Elbaz, D. 2001, ApJ, 556, 562
Daddi, E. et al. 2004, ApJ, 617, 746
Daddi, E. 2007, ApJ, 670, 156
Dekel, A. 2009, Nature, 457, 451
Egami, E. 2010, A&A, 518, L12
Elbaz, D. 2001, A&A, 518, L29
Ellingson, E., Yee, H. K. C., Bechtold, J., & Elston, R. 1996, ApJ, 466, L71
Erb, D. K., Shapley, A. E., Pettini, M., Steidel, C. C., Reddy, N. A., Adelberger, K. L. 2006a, ApJ, 644, 813
Erb, D. K., Steidel, C. C., Shapley, A. E., Pettini, M., Reddy, N. A., Adelberger, K. L. 2006b, ApJ, 646, 107
Erb, D. K., Steidel, C. C., Shapley, A. E., Pettini, M., Reddy, N. A., Adelberger, K. L. 2006c, ApJ, 647, 128
Fazio, G. G. et al. 2004, ApJS, 154, 10
Finkelstein, S. L. et al. 2009, ApJ, 700, 376
Förster Schreiber, N. M. et al. 2009, ApJ, 706, 1364
Gilbank, D. G., Baldry, I. K., Balogh, M. L., Glazebrook, K.,& Bower, R. G. 2010, MNRAS, 405, 2594
Gilbank, D. G., Gladders, M. D., Yee, H. K. C.,& Hsieh, B. C. 2011, AJ, 141, 94
Gonzaga, S., Biretta, J. et al. 2010, HST WFPC2 Data Handbook, v. 5.0, ed., Baltimore, STScI
Hainline, K. N., Shapley, A. E., Kornei, K. A., Pettini, M., Buckley-Geer, E., Allam, S. S., & Tucker, D. L. 2009, ApJ, 701, 52
Hennawi, J. F. et al. 2008, AJ, 135, 664
Kennicutt, Jr., R. C. 1998, ARA&A, 36, 189
Kewley, L. J., & Dopita, M. A. 2002, ApJS, 142, 35
Kim, K.-T., & Koo, B.-C. 2001, ApJ, 549, 979
Koester, B. P. et al. 2010, ApJ, 723, L73
Law, D. R. et al. 2007, ApJ, 656, 1
Lilly, S. J., Carollo, C. M., & Stockton, A. N. 2003, ApJ, 597, 730
Lin, H. et al. 2009, ApJ, 699, 1242
Madau, P. 1995, ApJ, 441, 18
Mannucci, F. et al. 2009, MNRAS, 398, 1915
Maraston, C., Pforr, J., Renzini, A., Daddi, E., Dickinson, M., Cimatti, A., & Tonini, C. 2010, MNRAS, 407, 830
Marchesini, D., van Dokkum, P. G., Förster Schreiber, N. M., Franx, M., Labbé, I.,& Wuyts, S. 2009, ApJ, 701, 1765
McLean, I. S. et al. 1998, Society of Photo-Optical Instrumentation Engineers (SPIE) Conference Series, 3354, 566
Meurer, G. R., Heckman, T. M., & Calzetti, D. 1999, ApJ, 521, 64
Moustakas, J., Kennicutt, Jr., R. C., & Tremonti, C. A. 2006, ApJ, 642, 775
Moustakas, J., Kennicutt, Jr., R. C., Tremonti, C. A., Dale, D. A., Smith, J.-D. T., & Calzetti, D. 2010, ApJS, 190, 233
Noeske, K. G. et al. 2007, ApJ, 660, L43
Nordon, R. 2001, A&A, 518, L24
Oesch, P. A. et al. 2010, ApJ, 725, L150
Osterbrock, D. E. 1989, Astrophysics in Gaseous Nebulae and Active Galactic Nuclei
Pannella, M. et al. 2009, ApJ, 698, L116
Papovich, C., Dickinson, M., Ferguson, H. C. 2001, ApJ, 559, 620
Papovich, C. et al. 2007, ApJ, 668, 45
Peng, C. Y., Ho, L. C., Impey, C. D., & Rix, H.-W. 2010, AJ, 139, 2097
Prevot, M. L., Lequeux, J., Prevot, L., Maurice, E., & Rocca-Volmerange, B. 1984, A&A, 132, 389
Reddy, N. A. et al. 2006, ApJ, 644, 792
Reddy, N. A., & Steidel, C. C. 2009, ApJ, 692, 778
Reddy, N. A., Erb, D. K., Pettini, M., Steidel, C. C., & Shapley, A. E. 2010, ApJ, 712, 1070
Renzini, A., Ciotti, L. 1993, ApJ, 416, L49
Rex, M. 2010, A&A, 518, L13
Rieke, G. H. et al. 2004, ApJS, 154, 25
Rieke, G. H., Alonso-Herrero, A., Weiner, B. J., Pérez-González, P. G., Blaylock, M., Donley, J. L.,& Marcillac, D. 2009, ApJ, 692, 556
Rigby, J. R. et al. 2008, ApJ, 675, 262
Rigby, J. R., Wuyts, E., Gladders, M., Sharon, K.,& Becker, G. D. 2011, ApJ, 732, 59
Rujopakarn, W., Rieke, G. H., Eisenstein, D. J., & Juneau, S. 2011, ApJ, 726, 93
Rujopakarn, W., Rieke, G. H., Weiner, B. J., Rex, M., Walth, G. L., & Kartaltepe, J. S. 2011, arXiv1107.2921
Salim, S. et al. 2007, ApJS, 173, 267
Schlegel, D. J., Finkbeiner, D. P.,& Davis, M. 1998, ApJ, 500, 525
Seaton, M. J. 1979, MNRAS, 187, 73P
Seitz, S., Saglia, R. P., Bender, R., Hopp, U., Belloni, P.,& Ziegler, B. 1998, MNRAS, 298, 945
Shapley, A. E., Steidel, C. C., Adelberger, K. L., Dickinson, M., Giavalisco, M., & Pettini, M. 2001, ApJ, 562, 95
Shapley, A. E. et al. 2005, ApJ, 626, 698
Sharon, K., Gladders, M. D., Rigby, J. R., Wuyts, E., Koester, B. P., Bayliss, M. B., Barrientos, L. F. 2011, in preparation
Shi, F., Zhao, G., & Liang, Y. C. 2007, A&A, 475, 409
Siana, B., Teplitz, H. I., Chary, R.-R., Colbert, J., & Frayer, D. T. 2008, ApJ, 689, 59
Siana, B. et al. 2009, ApJ, 698, 1273
Smail, I. et al. 2007, ApJ, 654, L33
Steidel, C. C., Shapley, A. E., Pettini, M., Adelberger, K. L., Erb, D. K., Reddy, N. A., & Hunt, M. P. 2004, ApJ, 604, 534
Teplitz, H. I. et al. 2000, ApJ, 533, L65
Tremonti, C. A. et al. 2004, ApJ, 613, 898
van der Burg, R. F. J., Hildebrandt, H., & Erben, T. 2010, A&A, 523, A74
van der Werf, P. P., Knudsen, K. K., Labbé, I., & Franx, M. 2001, Deep Millimeter Surveys: Implications for Galaxy Formation and Evolution, ed. J. D. Lowenthal & D. H. Hughes, 103+
Wuyts, E. et al. 2010, ApJ, 724, 1182
Wuyts, S. et al. 2007, ApJ, 655, 51
Wuyts, S. et al. 2011, arXiv1106.5502
Yee, H. K. C., Ellingson, E., Bechtold, J., Carlberg, R. G., Cuillandre, J.-C. 1996, AJ, 111, 1783
Zaritsky, D., Kennicutt, R. C., & Huchra, J. P. 1994, ApJ, 420, 87